Journal of Applied Electrochemistry **30**: 1397–1404, 2000.

Effect of molten carbonate composition on oxygen reduction under pressurized conditions: cyclic voltammetry and equivalent circuit analysis[†]

M. MOHAMEDI, Y. HISAMITSU, Y. ONO, T. ITOH and I. UCHIDA
Department of Applied Chemistry, Graduate School of Engineering, Tohoku University, 07 Aramaki-Aoba, Aoba-ku, Sendai, 980-8579, Japan

Received 31 July 1999; accepted in revised form 4 January 2000

Key words: molten carbonate, oxygen reduction, pressurization, solubility

Abstract

The oxygen reduction mechanism was investigated in carbonate melts of variable composition ranging from the eutectics Li–K, Li–Na to ternary Li–Na–K melts. The effect of pressure on electrode kinetics was also examined. Cyclic voltammetry, convolution voltammetry and electrochemical impedance spectroscopy have shown that oxygen reduction is mass-transfer limited in all melt compositions investigated. It was also found that pressurizing increased the concentration of oxygen electroactive species. To gain information about the reaction mechanism, the impedance spectra have been fitted to four possible equivalents circuits: (i) Randles circuit, (ii) Randles circuit extended by a parallel *RC* circuit due to film formation, (iii) Gerisher (homogeneous reaction) impedance, and (iv) Modified Randles circuit. The discussion of the results is based on careful analysis of fit quality and meaningfulness of fit parameters.

1. Introduction

The molten carbonate fuel cell (MCFC) is one of the most effective energy conversion systems but the state-of-the-art needs further advances to increase cost-effectiveness and allow commercial production.

The optimization of porous electrode structure (especially for the cathode) requires a deeper understanding of oxygen electrode kinetics in molten carbonate. This understanding must be correlated to melts of variable composition (ranging from eutectic and Li-rich Li–K melts via ternary Li–Na–K eutectic to various Li–Na compositions) and the effect of additives. The effect of pressure on electrode kinetics is also of particular importance and requires an insight into the reaction mechanism. Secondly, an effective and accurate mathematical model for porous electrode performance is required. Finally, to apply such a model, more data than presently available are required for the physical and transport properties (solubility, diffusivity, ionic mobilities) of oxygen containing carbonate melts.

The reaction mechanism of the oxygen reduction in molten carbonates is still a matter of controversy. The most probable paths are shown below [1–4]:

(i) *Peroxide mechanism*

$$O_2 + 2\,CO_3^{2-} \leftrightarrow 2\,O_2^{2-} + 2\,CO_2 \tag{1a}$$

$$O_2^{2-} + 2\,CO_2 + 2\,e^- \rightarrow 2\,CO_3^{2-} \tag{1b}$$

(ii) *Superoxide mechanism*

$$3\,O_2 + 2\,CO_3^{2-} \leftrightarrow 4\,O_2^- + 2\,CO_2 \tag{2a}$$

$$O_2^- + 2\,CO_2 + 3\,e^- \rightarrow 2\,CO_3^{2-} \tag{2b}$$

(iii) *Percarbonate mechanism*

$$O_2 + 2\,CO_3^{2-} \leftrightarrow 2\,CO_4^{2-} \tag{3a}$$

$$CO_4^{2-} + CO_2 + 2\,e \rightarrow 2\,CO_3^{2-} \tag{3b}$$

The predominant reaction mechanism depends on the gas composition, the temperature as well as on the cationic composition of the molten carbonate electrolyte. Reactions 1(b), 2(b) and 3(b) are most likely split into sub reactions as proposed in the literature [1–4]. Moreover, the existence of different oxygen reduction mechanisms should be imagined under operating conditions, a mention is given in [5] where a combination of peroxide or superoxide species may be possible.

In this work oxygen reduction kinetics were experimentally investigated in various melts by electrochemical impedance spectroscopy (EIS), cyclic voltammetry and convolution voltammetry at gold flag electrodes under atmospheric and pressurized conditions.

[†] Dedicated to the memory of Daniel Simonsson

2. Experimental details

Melt purification, gas handling, and cell assembly have been described previously [6–8]. The working electrode was a gold flag (0.39 cm^2), which was fully immersed in the melt. The counter electrode was a coiled gold wire (1 mm dia., 15 cm length). The reference electrode was a gold flag quasi-reference. Electrochemical measurements were carried out in alkali carbonates of different electrolyte compositions. The working temperature was fixed to 923 K and was monitored by an alumel–chromel thermocouple sheathed in a protective alumina tube.

Premixed O_2/CO_2 = 90/10 supplied by Sumitomo Seika Chemicals was used as the gas oxidant. The total pressure was varied from 1 to 5 atm.

Cyclic voltammetric measurements were performed using a Solartron 1286 Electrochemical Interface connected to Nicolet 310 digital oscilloscope. Data were transferred to a personal computer for further processing. Convolution voltammetry or semi-integral procedure was carried out on the basis of Oldham's G1 and G2 algorithms [9].

Impedance measurements were carried out with the aid of a 1260 Solartron frequency response analyser. The spectra were recorded at the open-circuit potential, using a superimposed voltage signal of 10 mV amplitude in the frequency range 1 Hz to 10 kHz.

The quantitative analysis of the experimental impedance data was performed using a nonlinear least squares minimization method called 'Equivcrt' developed by Boukamp [10]. This program simultaneously fits the imaginary and the real parts of the impedance data and provides uncertainty estimates for all estimated parameters, thus obtaining the optimum fit to the measured dispersion data.

3. Results and discussion

3.1. *Cyclic voltammetry and semiintegral analysis*

The cathodic evolution of the voltammetric curves at a gold flag electrode is shown as function of some electrolyte compositions in Figure 1. In all cases, only one peak was observed in this potential range. We have observed that within 0.1–1 V s^{-1} scan rate range the current peaks were proportional the square root of the scan rate indicating that the electrochemical process is under diffusion-control. Diffusion control, as indicated by square root dependence, has also been reported in the literature [11–13]. The effect of the total pressure is shown in a sample plot (Figure 2) related to voltammograms recorded in the Li_2CO_3–Na_2CO_3–K_2CO_3 (26.7–23.3–50 mol %). Pressurization increases the current peaks due to increase in the concentration of the electroactive species. The same effect was observed for all the electrolyte compositions considered.

Semiintegral voltammetry was carried out on the voltammograms of Figure 2 and the results are shown in Figure 3. The semiintegral curves exhibit a limiting value in the high cathodic potential domain. The presence of this plateau is a strong indication that the reduction of oxygen is under diffusion control [14].

It has been demonstrated that under purely-diffusion controlled conditions, when the concentration of Ox species in the vicinity of the electrode surface becomes zero, the semiintegral curve reaches its limiting value expressed by

$$m^* = nFAC_i^0\sqrt{D_i} \tag{4}$$

with C_i^0 being the equilibrium or bulk concentration and D_i the diffusion coefficient of species i.

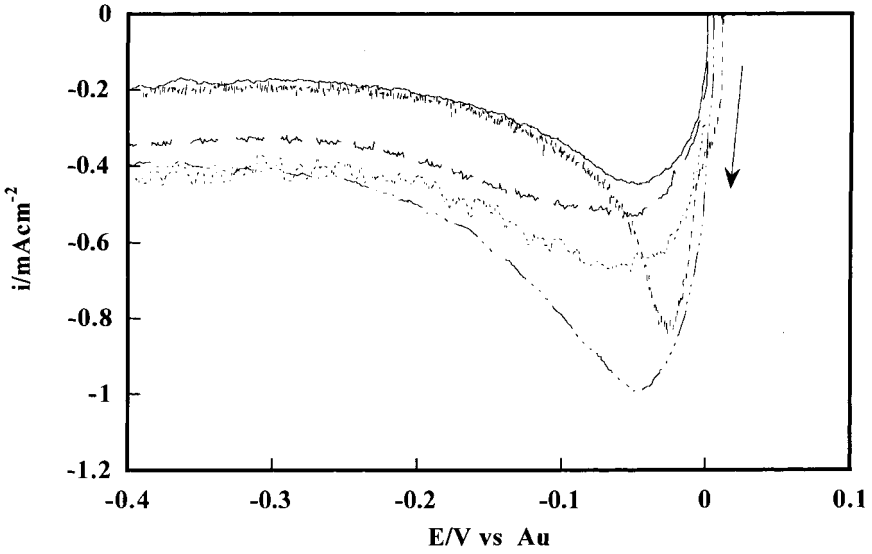

Fig. 1. Effect of melt composition on voltammograms run at gold flag electrode under 1 atm of O_2/CO_2 = 90/10 at 923 K. Scan rate 1 V s^{-1}. (Li–Na–K)CO_3: (- - - -) 53–47–0; (—— -) 62–0–38; (——) 63–27–10; (·····) 48–12–40 and (— - - -) 26.7–23.3–50.

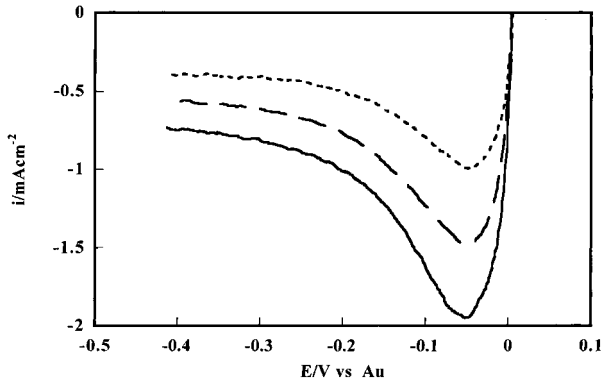

Fig. 2. Effect of the total pressure of O_2/CO_2 = 90/10 on the voltammograms run at gold flag electrode dipped in (26.7–23.3–50) mol % (Li–Na–K)CO_3. T = 923 K, Scan rate 1 V s^{-1}. P_{total}: (- - -) 1, (– – –) 3 and (——) 5 atm.

Equation 4 is valid whether or not the electrochemical system is reversible [14]. Furthermore, the m^* value is independent of the scan rate thus assuring precise determination of the diffusion coefficient. The mass-transport parameter, $C_i^0\sqrt{D_i}$, as determined by means of Equation 4 (assuming n = 2) is shown in Table 1 for some electrolyte compositions.

3.2. *Electrochemical impedance spectroscopy (EIS)*

We have tested several equivalent circuits in attempting to fit the experimental data. In many cases we obtained a good match between the measured and calculated diagrams. However, most of the equivalent circuits were based on fit parameters involving 9 or more adjustable parameters. Given enough fit parameters low fit errors are found when fitting to almost any data set. Consequently, we retained only equivalent circuits that are more consistent with the data and the physico-chemical properties of the system.

Experimental impedance data were modelled using the equivalent circuits illustrated in Figure 4 where R_s is the solution resistance (Ω); C_{dl} is the double layer capacitance (farad); R_{ct} is the charge transfer resistance due to heterogeneous electrochemical reactions. It is

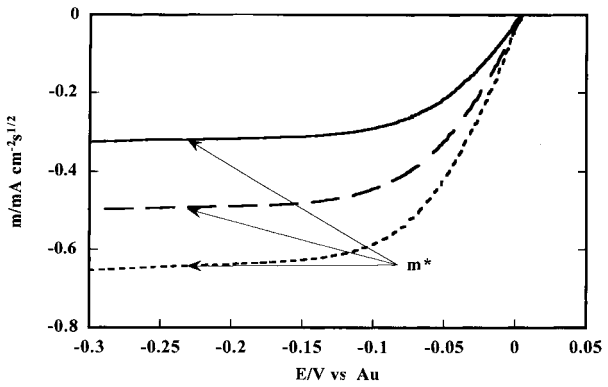

Fig. 3. Semiintegral curves corresponding to voltammograms presented in Figure 2. P_{total}: (——) 1, (– – –) 3 and (- - -) 5 atm.

Table 1. Mass transport parameter $C_i^0\sqrt{D_i}$ determined from the semiintegral analysis using Equation 4 (assuming n = 2)

Li–Na–K /mol %	$C_i^0\sqrt{D_i} \times 10^9$ /mol cm^{-2} s$^{-0.5}$	
	1 atm	3 atm
53–47–0	0.88	1.10
62–0–38	1.19	1.66
48–42–10	1.35	2.45
26.7–23.3–50	1.66	2.54
63–27–10	0.72	1.14

also related to the exchange current density, i_0, according to $R_{ct} = RT/nFi_0$; W is the Warburg impedance element that represents the semi-infinite diffusion processes of reactants and or/products; G is the Gerisher impedance element that represents the impedance due to homogeneous chemical reactions preceded or followed by a charge transfer reaction; and $Q(s^n/\Omega)$ is a constant phase element-unit (CPE). The CPE is a diffusion-related element. Its impedance representation, Z_{CPE} has the following form:

$$Z_{CPE} = [Q(j\omega)^n]^{-1} \tag{5}$$

where Q is a constant containing the diffusion coefficient, ω is the radial frequency ($2\pi f$) and n is a number between −1 and 1. The CPE may be interpreted as different electronic components depending on the n value. It represents a resistor, R, when n = 0, a capacitor, C, when n = 1, and an inductor, L, when n = −1 and a Warburg when n = 0.5. When n = 0.5 the Warburg coefficient, σ can be determined as

$$\sigma = \frac{1}{\sqrt{2}Q} = \frac{RT}{n^2F^2\sqrt{2}}\sum_i \frac{1}{C_i^0\sqrt{D_i}} \tag{6}$$

Nishina et al. [15] employed the equivalent circuit of Figure 4(a) (the Randles–Ershler circuit) to fit a.c. impedance measurements of MCFC electrode reactions at an Au flag electrode. The fit confirmed that the superoxide path (Reactions 2(a) and (b)) is dominant in the reduction of oxygen in Li_2CO_3–K_2CO_3 eutectic melts, while the simultaneous diffusion of O_2^- and CO_2 limit the reaction-related mass transfer.

Makkus [4] included in the Randles–Ershler circuit a chemical reaction resistance (Gerisher resistance, Figure 4(b)) in order to fit the hypothesis that percarbonate, CO_4^{2-}, is formed (Reactions 3(a) and (b)) which acts as the dominant source of diffusion resistance in the cathode reaction.

The circuit in Figure 4(c) takes into account the presence of a thin film at the gold electrode. The thin film here was attributed to the presence of oxygen-containing species adsorbed at the electrode surface. The involvement of adsorbed oxygen during the reduction of oxygen in molten carbonate has been previously reported [16, 17]. Recently, we have demonstrated, by means of the semiintegral method, the involvement of adsorption

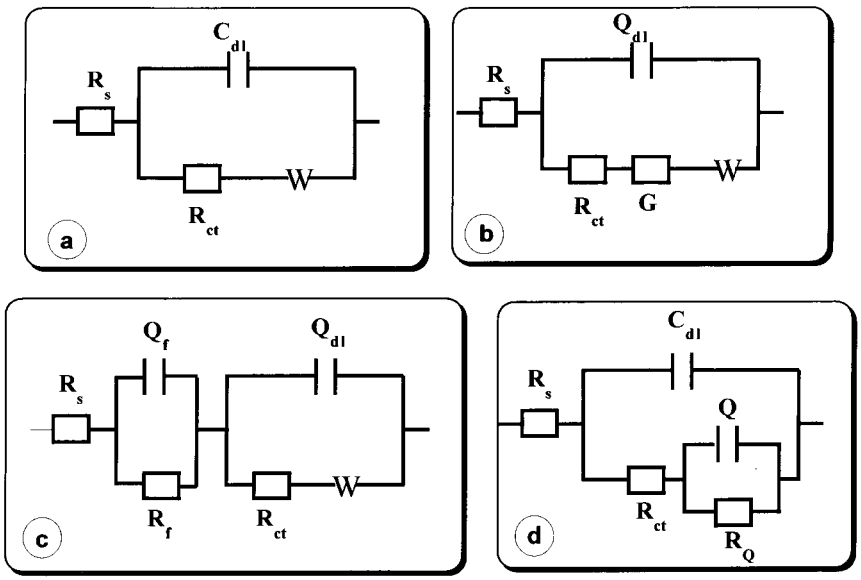

Fig. 4. Equivalent circuits used to fit the impedance spectra obtained at a gold flag electrode dipped in molten carbonates at 923 K. (a) Randles circuit, (b) Gerisher circuit, (c) thin film circuit and (d) Randles modified circuit.

processes during the reduction of oxygen at gold in molten Li–Na carbonate eutectic [18].

To study the difference between the four equivalent circuits of Figure 4, there are accurate ways to get an indication on how well the modeling function reproduces the actual data set, first, by observing the parameter values and their relative error estimate (in %). The chi-square function also gives a good indication of the quality of the fit. A value of 10^{-5} or less for chi-squared indicates a reasonable good fit.

Secondly, the actual data set can best be observed in a graph of the relative residuals, $\Delta_{\mathrm{re},i}$ and $\Delta_{\mathrm{im},i}$ against log ω. Following Boukamp [19] the residuals are defined by

$$\Delta_{\mathrm{re},i} = \frac{Z_{\mathrm{re},i} - Z_{\mathrm{re}}(\omega_i)}{|Z(\omega_i)|} \quad \text{and} \quad \Delta_{\mathrm{im},i} = \frac{Z_{\mathrm{im},i} - Z_{\mathrm{im}}(\omega_i)}{|Z(\omega_i)|} \tag{7}$$

where $Z_{\mathrm{re},i}$ and $Z_{\mathrm{im},i}$ the real and imaginary parts of the ith data set (at frequency ω_i) and $Z_{\mathrm{re}}(\omega_i)$ and $Z_{\mathrm{im}}(\omega_i)$ the real and imaginary parts of the modelling function for ω_i. $|Z(\omega_i)|$ is the vector length of the modelling function. An optimum fit is obtained when the residuals are scattered randomly around the log ω axis. When the residuals show a systematic deviation from the horizontal axis, for example, by forming a 'trace' around, above, or below the log ω axis the fitting model is not adequate. This may be due to several factors, among them, (i) the data contain systematic errors; these can be due to the measuring setup and equipment, aging of the sample, slow change in the sample temperature, etc., (ii) the chosen modelling function is not appropriate. It is important to be able to distinguish between causes (i) and (ii). Here, the Kramers–Kronig (K–K) transforms can be employed to indicate whether the data are at fault or the equivalent circuit is inadequate. The K–K relations dictate that the real and imaginary part of any immittance function are interdependent, provided that the following conditions are met: (i) causality (the response depends on excitation signal only); (ii) linearity (only the first order term must be present in the response signal); (iii) stability (the system may not change with time).

The interdependence between the real and imaginary parts of the dispersion is presented in K–K transform integrals. When the imaginary part is known, the real part can be obtained through the K–K transform integral [19]

$$Z_{\mathrm{re}}(\omega) = R_{\mathrm{s}} + \frac{2}{\pi}\int_0^{\infty} \frac{xZ_{\mathrm{im}}(x) - \omega Z_{\mathrm{im}}(\omega)}{x^2 - \omega^2}\,\mathrm{d}x \tag{8}$$

while the imaginary part can be obtained

$$Z_{\mathrm{im}}(\omega) = \frac{2\omega}{\pi}\int_0^{\infty} \frac{Z_{\mathrm{re}}(x) - Z_{\mathrm{re}}(\omega)}{x^2 - \omega^2}\,\mathrm{d}x \tag{9}$$

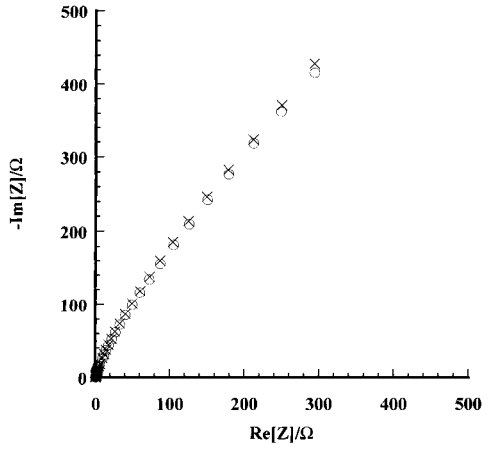

Fig. 5. Exemplary plot of Kramers–Kronig transform (×) of the measured (○) impedance spectra. Diagram recorded at gold electrode in (63–27–10) mol % (Li–Na–K)CO_3. T = 923 K.

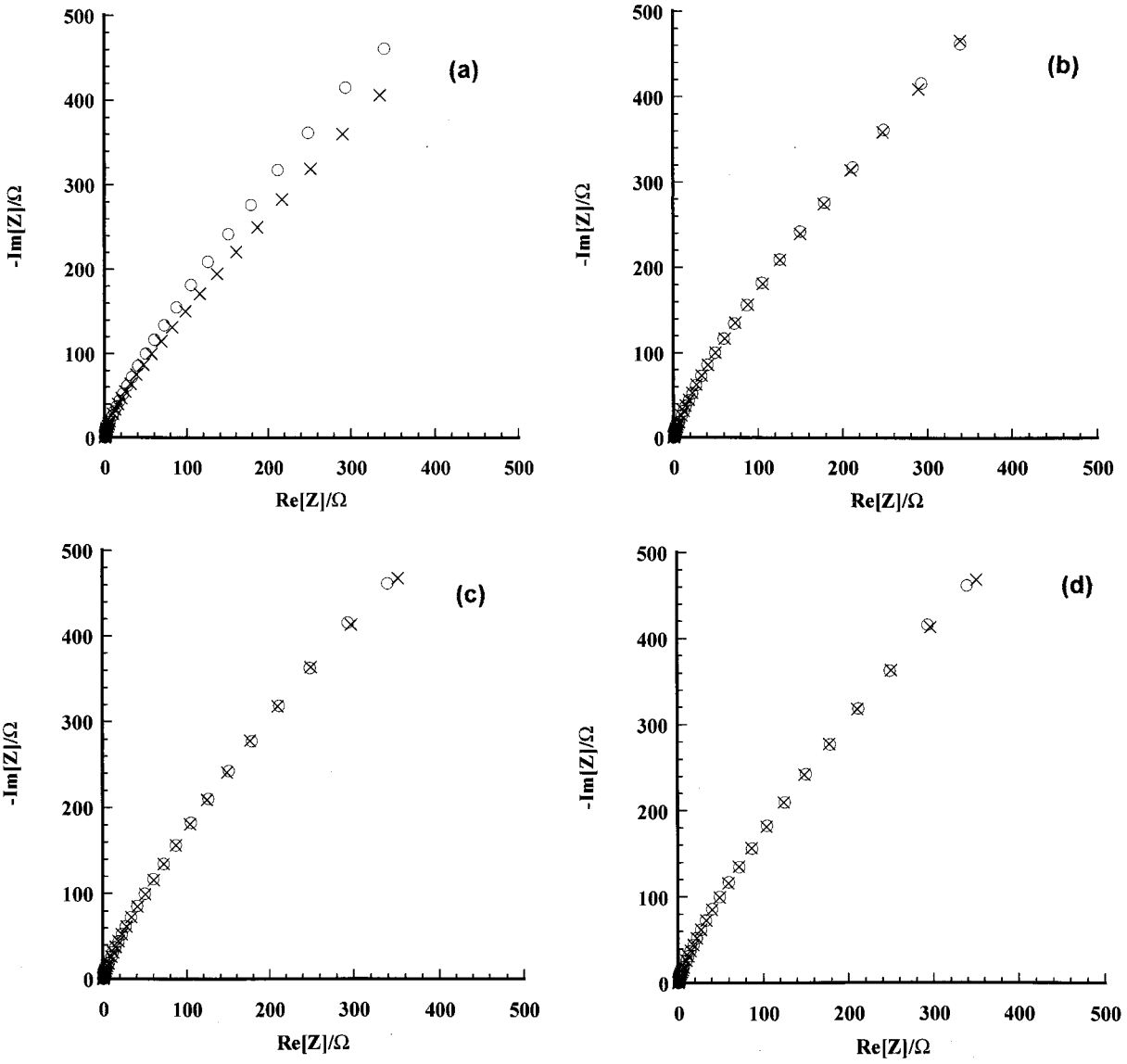

Fig. 6. Measured impedance spectra compared to calculated ones following the equivalents circuits shown in Figure 4. Experimental diagram recorded in (63–27–10) mol % (Li–Na–K)CO_3. T = 923 K. Key: (○) measurement; (×) fitted with Randles circuit (a), Gerisher circuit (b), thin film circuit (c) and Randles modified circuit (d).

The data from a stable system must comply with these transformation rules. If the imaginary part does not appear to be the same as the real-to-imaginary transform, Equation 8 or vice versa, then the data set must be considered non K–K transformable, that is, time varying or nonlinear.

The K–K transform was applied to the experimental impedance data. A typical example is shown in Figure 5.

Table 2. Parameters fitting and their relative error estimates for the four equivalents circuits presented in Figure 4

Randles circuit $\chi^2 = 6.13 \times 10^{-3}$		Gerisher circuit $\chi^2 = 4.25 \times 10^{-4}$		Thin film circuit $\chi^2 = 1.83 \times 10^{-4}$		Randles modified circuit $\chi^2 = 4.1 \times 10^{-5}$	
Parameter	Rel. error /%	Parameter	Rel. error /%	Parameter	Rel. error /%	Parameter	Rel. error /%
R_s = 0.32 Ω	6.81	R_s = 0.25 Ω	57.48	R_s = 0.26 Ω	3.85	R_s = 0.29 Ω	0.91
$C_{dl} = 4.4 \times 10^{-5}$ F	*	$Q = 7.7 \times 10^{-5}$ s^n Ω^{-1}	63.77	$Q = 8.2 \times 10^{-5}$ s^n Ω^{-1}	31.75	$C_{dl} = 3.8 \times 10^{-5}$ F	0.64
$R_{ct} = 10^{-16}$ Ω	*	n = 0.93	10.28	n = 0.93	8.09	R_{ct} = 4.5 Ω	8.68
$W = 6.8 \times 10^{-4}$ Ω^{-1} $s^{0.5}$	2.57	$R_{ct} = 10^{-16}$ Ω	*	R_{ct} = 11 Ω	262.6	$R_Q = 4.8 \times 10^3$ Ω	5.58
		$G = 6 \times 10^{+15}$	*	$W = 7.1 \times 10^{-4}$ Ω^{-1} $s^{0.5}$	93.37	$Q = 4.6 \times 10^{-4}$ s^n Ω^{-1}	0.89
		$k = 10^{+16}$ s^{-1}	*	R_Q = 264 Ω	531	n = 0.60	0.31
		$W = 5.5 \times 10^{-4}$ Ω^{-1} $s^{0.5}$	3.95	$Q = 1.3 \times 10^{-3}$ s^n Ω^{-1}	190.5		
				n = 0.92	68.5		

* indicates that the relative error was too large

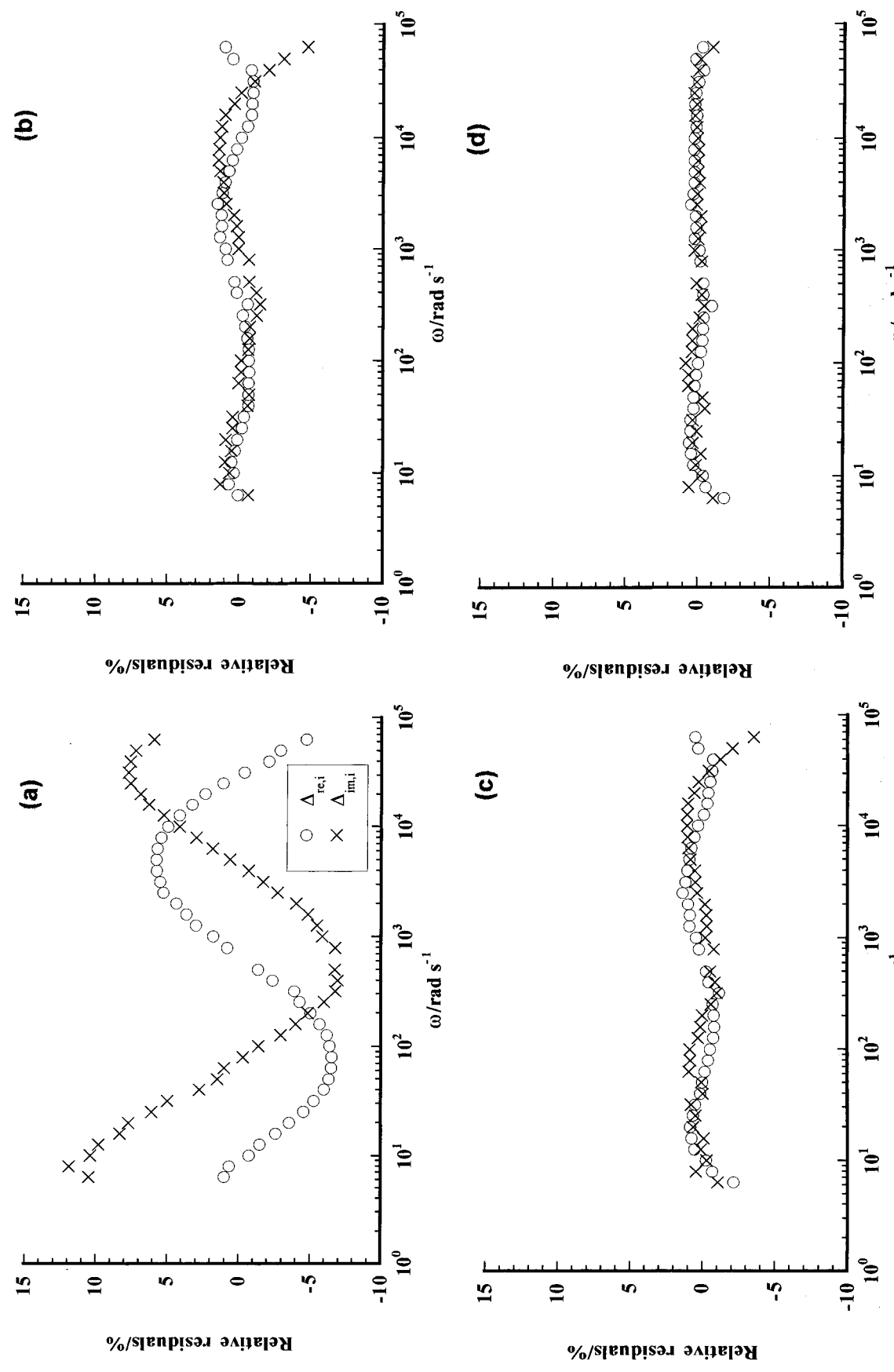

Fig. 7. Relative residuals plots for the fits presented in Figure 6. Relative residuals for the real and imaginary parts calculated using Equation 7. Key: (a) Randles circuit, (b) Gerisher circuit, (c) thin film circuit and (d) Randles modified circuit.

The data are free of error for the frequency range used in this work. We have verified that all impedance data recorded for different electrolyte compositions were K–K transformable. Subsequently, the experimental data were fitted to the equivalent circuits of Figure 4. The results are illustrated in Figure 6 and the fitting parameter values with their relative error estimates are summarized in Table 2.

At first glance, it is seen from Figure 6 that the fitting appears to be comparable for all the equivalent circuits except for the Randles-circuit. For the latter, the systematic application of the Boukamp fitting program showed that the classical Warburg element W (Figure 4(a)) had to be substituted by a CPE-unit (Figure 4(d)). When examining data reported in Table 2, the best fit obtained by the circuit with the most adjustable parameters is the modified Randles-circuit (Figure 4(d)). Since it exhibited the lowest chi-square function and the lowest relative error estimates of the parameter values (<10%), and the corresponding parameters gave rise to realistic estimates of process parameters. More convincing, are the relative-residual plots for the fit results shown in Figure 7. There is evidently a trace in the real and the imaginary component for the circuits (a), (b) and (c) of Figure 4, where the residuals are greater than 2%, whereas the Randles-modified circuit shows a residual error well within 0.5–1%. Consequently, hereafter the equivalent circuit of Figure 4(d) was adopted and fitted to all experimental impedance spectra recorded for different electrolyte compositions and under different pressures. It might be argued that the reaction mechanism may change with changing electrolyte composition or pressure and, under these conditions, the equivalent circuit of Figure 4(d) may not be valid. We must emphasize that all the impedance diagrams were similar in shape to that represented in Figure 5 and we have, of course, fitted these data with the four models of Figure 4; the results suggest that the modified Randles circuit adequately describes the responses. Typical comparison of experimental and calculated data related to various electrolyte compositions represented as Nyquist plots are shown in Figure 8.

The double layer capacitance determined from the fitting procedure is depicted in Figure 9. It can be seen that pressurization has no significant effect on the value of the double layer capacitance.

The exponent n (Equation 5) was found to lie between 0.5 and 0.6 as observed on Figure 10. This means that the preexponential factor, Q, of the CPE-unit in Figure 4(d) acts as a Warburg response. This indicates that the kinetics of oxygen reduction are limited by the diffusion of the reduction products. Therefore, the Warburg coefficient σ was determined from the Q values via Equation 6. The results are listed in Table 3. In agreement with the results of voltammetry (Section 3.1) it is seen that, for a given melt composition, the effect of pressurizing is to decrease significantly σ, thus increasing $C_i^0\sqrt{D_i}(\sim 1/\sigma)$.

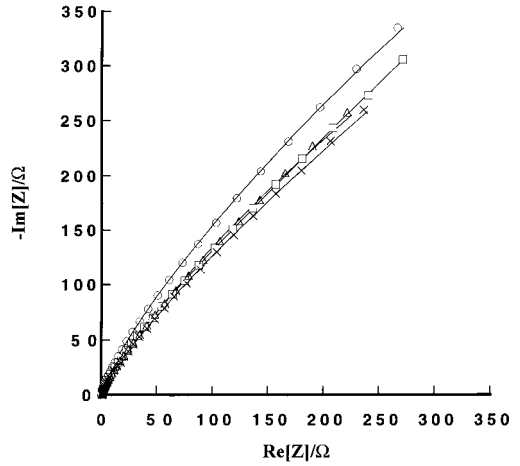

Fig. 8. Experimental impedance spectra recorded in some electrolyte compositions compared to impedance spectra calculated using the equivalent circuit of Figure 4(d). Key: (○) (53–47–0), (□) (26.7–23.3–50), (△) (62–0–38), (×) (35.3–20.5–44.1) mol % (Li–Na–K)CO_3. Under 1 atm of O_2/CO_2 = 90/10 at 923 K.

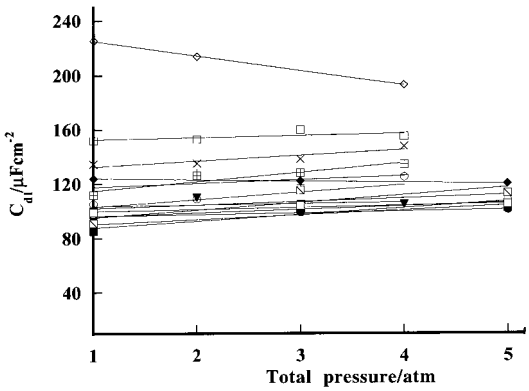

Fig. 9. Effect of the total pressure of O_2/CO_2 = 90/10 on the double layer capacitance in various melt composition at 923 K. (Li–Na–K)CO_3: (○) 53–47–0; (□) 62–0–38; (◇) 32–28–40; (×) 48–42–10; (+) 43.5–31.5–25; (△) 20–30–50; (●) 25–25–50; (■) 26.7–23.3–50; (◆) 30–45–25; (▲) 35.3–20.6–44.1; (▼) 40–0–60; (○) 41.4–24.1–34.5; (⧅) 48–12–40; (⊞) 60–15–25; and (⊡) 63–27–10 mol %.

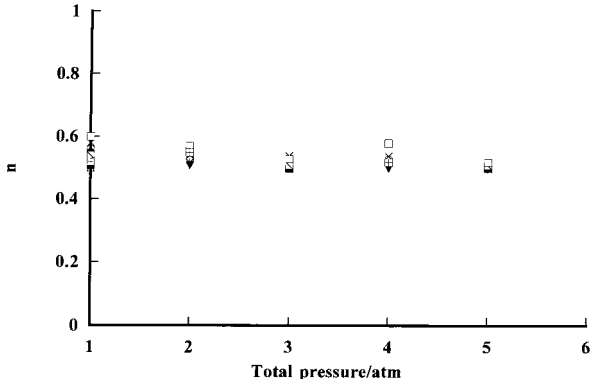

Fig. 10. Values of the exponent n corresponding to the constant phase element (CPE) of Figure 4(d) determined by the fitting program. (Li–Na–K)CO_3: (○) 53–47–0; (□) 62–0–38; (◇) 32–28–40; (×) 48–42–10; (+) 43.5–31.5–25; (△) 20–30–50; (●) 25–25–50; (■) 26.7–23.3–50; (◆) 30–45–25; (▲) 35.3–20.6–44.1; (▼) 40–0–60; (○) 41.4–24.1–34.5; (⧅) 48–12–40; (⊞) 60–15–25; and (⊡) 63–27–10 mol %.

Table 3. Warburg coefficient σ, for different melt compositions and under pressurized conditions
σ was evaluated from Q (determined by the fitting program) using Equation 5

Li–Na–K /mol %	$\sigma/\Omega\ cm^2\ s^{0.5}$				
	1 atm	2 atm	3 atm	4 atm	5 atm
53–47–0	527.3	459.6	424	367.7	–
62–0–38	315	231.7	215	142	–
32–28–40	156.7	133	–	109	–
48–42–10	544	383	311.6	273	–
43.5–31.5–25	270	154	123	110.7	–
20–30–50	228	–	198	–	141
25–25–50	257.7	–	159.4	–	168
26.7–23.3–50	320.7	–	230	–	201
30–45–25	220.6	–	156	–	150.7
35.3–20.6–44.1	290.6	–	222	–	184
40–0–60	160	124.8	121	114	–
41.4–24.1–34.5	244	–	145	–	116
48–12–40	282	–	161	–	132.6
60–15–25	361	233.7	195.6	165	–
63–27–10	597	–	281.7	–	230

The EIS results shows that the oxygen reduction kinetics in Li–Na–K carbonate melts are mass-transfer limited, and that the impedance value depends on the gas pressures and on the carbonate composition. For a given electrolyte composition, pressurization reduced the diffusion resistance of the reactant species.

The Warburg coefficient derived from EIS measurements at up 5 atm pressure indicated that the mass-transfer limitation is less in Li–Na–K melt than in Li–K melt, but its pressure dependence is more pronounced. This may be attributed to diffusion control by the superoxide ion $\left(O_2^-\right)$ and CO_2.

In order to optimize the electrolyte composition, the next step will be to model the response of the Warburg coefficient with different melt compositions taking into account the effects of the total pressure. This work is under way.

Acknowledgements

This work was supported by the International Joint Research Grant (Advanced MCFC) and the Proposal-Based-Immediate Effect R&D Promotion Program no. 98Z31-011 from the New Energy and Industrial Technology Development Organization (NEDO).

References

1. A.J. Appleby and S.B. Nicholson, *J. Electroanal. Chem.* **112** (1980) 71.
2. K. Yamada, T. Nishina, I. Uchida and J.R. Selman, *Electrochim. Acta* **38** (1993) 2405.
3. G.B. Dunks and D. Stelman, *Inorg. Chem.* **22** (1983) 2168.
4. R. Makkus, Doctoral thesis, Delft University of Technology, Delft, The Netherlands (1991).
5. M. Cassir, B. Malinowska, W. Peelen, K. Hemmmes and J.H.W. de Wit, *J. Electroanal. Chem.* **433** (1997) 195.
6. I. Uchida, T. Nishina, Y. Mugikura and K. Itaya, *J. Electroanal. Chem.* **206** (1986) 229.
7. I. Uchida, Y. Mugikura, T. Nishina and K. Itaya, *J. Electroanal. Chem.* **206** (1986) 241.
8. I. Uchida, T. Nishina, Y. Mugikura and K. Itaya, *J. Electroanal. Chem.* **209** (1986) 125.
9. K.B. Oldham, *J. Electroanal. Chem.* **121** (1981) 341.
10. B.A. Boukamp, 'Equivalent Circuit User's Manual' (University of Twente, 1989).
11. A.J. Appleby and S. Nicholson, *J. Electroanal. Chem.* **53** (1974) 105.
12. A.J. Appleby and S.B. Nicholson, *J. Electroanal. Chem.* **83** (1977) 309.
13. B.B. Dave, R.E. White, S. Srinivasan and A.J. Appleby, *J. Electrochem. Soc.* **138** (1991) 673.
14. M. Greness and K.B. Oldham, *Anal. Chem.* **44** (1972) 1121.
15. T. Nishina, I. Uchida and J.R. Selman, *J. Electrochem. Soc.* **141** (1994) 1191.
16. M. Matsumura and J.R. Selman, *J. Electrochem. Soc.* **139** (1992) 1255.
17. C-G. Lee, K. Yamada, T. Nishina and I. Uchida, *J. Electrochem. Soc.* **143** (1996) 2315.
18. M. Mohamedi, Y. Hisamitsu, Y. Ono, T. Itoh and I. Uchida, *J. Electrochem. Soc.* **147** (2000) 490.
19. B.A. Boukamp, *J. Electrochem. Soc.* **142** (1995) 1885.